

Article

Biomass Based N/O Codoped Porous Carbons with Abundant Ultramicropores for Highly Selective CO₂ Adsorption

Congxiu Guo ¹, Ya Sun ¹, Hongyan Ren ², Bing Wang ^{1,*}, Xili Tong ^{3,*}, Xuhui Wang ¹, Yu Niu ¹ and Jiao Wu ^{1,*}

¹ School of Electric Power, Civil Engineering and Architecture, Shanxi University, Taiyuan 030006, China; guocongxu@sxu.edu.cn (C.G.); 17835342913@163.com (Y.S.); wangxuhui@sxu.edu.cn (X.W.); niuyu@sxu.edu.cn (Y.N.)

² Jinzhong College of Information, Taigu 030800, China; renhongyan@jzci.edu.cn

³ State Key Laboratory of Coal Conversion, Institute of Coal Chemistry, Chinese Academy of Sciences, Taiyuan 030001, China

* Correspondence: wangbing@sxu.edu.cn (B.W.); tongxili@sxicc.ac.cn (X.T.); jiaow@sxu.edu.cn (J.W.)

Abstract: In this work, N/O codoped porous carbons (NOPCs) were derived from corn silk accompanied by Na₂CO₃ activation. The porous structures and surface chemical features of as-prepared carbon materials were tailored by adjusting the Na₂CO₃ mass ratio. After activation, the optimized sample (NOPC1) with abundant ultramicropores and pyrrolic N displays an enhanced CO₂ adsorption capacity of 3.15 mmol g⁻¹ and 1.95 mmol g⁻¹ at 273 K and 298 K at 1 bar, respectively. Moreover, this sample also exhibited high IAST selectivity (16.9) and Henry's law selectivity (15.6) for CO₂/N₂ at 298 K as well as moderate heat adsorption. Significantly, the joint effect between ultramicropore structure and pyrrolic N content was found to govern the CO₂ adsorption performance of NOPCs samples.

Keywords: biomass; corn silk; ultramicropore; nitrogen and oxygen co-doping; CO₂ adsorption



Citation: Guo, C.; Sun, Y.; Ren, H.; Wang, B.; Tong, X.; Wang, X.; Niu, Y.; Wu, J. Biomass Based N/O Codoped Porous Carbons with Abundant Ultramicropores for Highly Selective CO₂ Adsorption. *Energies* **2023**, *16*, 5222. <https://doi.org/10.3390/en16135222>

Academic Editors: Haris Ishaq and Liwei Zhang

Received: 14 June 2023

Revised: 4 July 2023

Accepted: 5 July 2023

Published: 7 July 2023



Copyright: © 2023 by the authors. Licensee MDPI, Basel, Switzerland. This article is an open access article distributed under the terms and conditions of the Creative Commons Attribution (CC BY) license (<https://creativecommons.org/licenses/by/4.0/>).

1. Introduction

Parallel to the massive consumption of fossil fuels, the continuous emissions of various air pollutants have led to global warming and resulted in a series of serious ecological issues. To alleviate these environmental problems, various technologies have been developed to inhibit CO₂ from releasing into the atmosphere, such as chemical absorption [1], physical absorption [2], membrane separation [3], cryogenic distillation [4] and others [5]. Among these technologies, physical absorption with the merits of a cost-effective process, including low equipment requirements, low power consumption and efficient regeneration [6,7], is considered one of the most competitive techniques to curb CO₂ emissions. To date, various porous materials, such as zeolite [8], porous organic polymers [9], mesoporous silica [10], graphene [11], metal-organic frameworks (MOFs) [12,13], covalent organic frameworks (COFs) [14] and porous carbons [15], have been developed as physical adsorbents for CO₂ capture. In this regard, porous carbons have been attracting greater attention due to their large specific surface area, adjustable porosity and surface functionality [15,16]. However, the low polarity of pristine porous carbons commonly causes poor adsorption selectivity of CO₂ over N₂ and low adsorption heat [6]. Activation is considered to be the optimal approach to improve the physicochemical properties of carbon materials, including physical activation and chemical activation. During physical activation, the porosity of carbon materials significantly increase through high temperature carbonization or partial gasification of a precursor. By contrast, during chemical activation, the activator can create a multi-scale porous structure for carbon materials via chemical etching under high temperatures [17,18]. Various activators have been widely used in the literature, such as KOH, NaOH, H₃PO₄, Na₂CO₃, K₂CO₃, ZnCl₂ and others [18,19]. Among these activators, KOH is the most frequently used as a chemical agent to modify various carbon materials to enhance

their CO₂ adsorption capacity. For instance, sucrose-derived porous carbons were prepared by adding different ratios of KOH and urea, and displayed a remarkable CO₂ uptake of 8.19 mmol g⁻¹ at 273 K and 1 bar [19]. Liu et al. [20] synthesized a category of porous carbon monoliths via a novel in-situ KOH activation methodology. The reported carbon monoliths had a high ultramicropore volume of 0.3 m³ g⁻¹ and therefore demonstrated remarkable static CO₂ uptake (5.0 mmol g⁻¹). Similarly, the N, S, and O co-doped porous carbons were fabricated via KOH activation of polybenzoxazine and exhibited a high CO₂ adsorption capacity of 7.04 mmol g⁻¹ and CO₂/N₂ selectivity of 27 at 273 K [21]. In fact, KOH activation can induce large amounts of micropores and small mesopores in carbon frameworks [22]. However, KOH activation can result in potentially serious environmental pollution and heavy corrosion damage to the experimental apparatus. In contrast, carbonate can simultaneously carry out chemical and physical activation of the carbon framework via the release of CO₂ at high temperatures [17]. For example, through a Na₂CO₃ assisted method, a 3D holey N-doped graphene with a large specific surface area of 1173 m² g⁻¹ was synthesized via fast pyrolysis of alanine [23]. Caglayan et al. demonstrated that the CO₂ mass uptake of carbon material activated by Na₂CO₃ was eight times high than that of the air oxidized and nitric acid oxidized counterparts [24].

Heteroatom doping, especially strongly electronegative atoms (such as N, O and P), can effectively improve the surface physical-chemical properties of carbon materials [25,26] and further enhance CO₂ adsorption performance. Substantially, incorporation of nitrogen into the carbon skeleton can provide abundant basic sites that may enhance the Lewis acid-base interaction between functional groups on the surface and acidic CO₂ molecules [19,22,27]. Furthermore, introduction of another heteroatom can increase the surface polarities of N-doped carbon materials [19], which is also conducive to CO₂ adsorption. For instance, N and P co-doped porous carbon was fabricated through pyrolysis of a highly-cross-linked triazine polymer and demonstrated an enhanced CO₂ adsorption capacity of 1.52 mmol g⁻¹ at 1 bar [28]. Similarly, N and O co-doped carbon nanotubes synthesized via coal pyrolysis activation achieved a remarkable CO₂ uptake capacity of 3.77 mmol g⁻¹ at 298 K and 1 bar [29]. In addition, micropores, especially ultramicropores (d < 1 nm), present a vital contribution to the adsorption capacity and adsorption selectivity of CO₂, while mesopores and macropores can reduce CO₂ transport resistance and accelerate CO₂ diffusion, respectively [29–31]. Therefore, rational design of carbon materials with a hierarchical porous structure of combined micropores, mesopores and macropores can optimize the adsorption performance of CO₂.

Biomass-derived porous carbons have received a great deal of attention for their physical adsorption of CO₂ considering their low cost, high accessibility, environmental sustainability and high chemical stability [32,33]. More significantly, heteroatom self-doping stemmed from the organic elements in plants that can be formed through chemical activation processes, and the multi-scale pores originated from biological structures with interconnected channels that can effectively increase the rates of CO₂ diffusion [33]. In a recent study, heteroatom-doped porous carbons derived from cornstalk [15], bamboo [34], tobacco stems [35], lotus stalks [36], hazelnut shells [37] and *Entada rheedii* shells [38] have been prepared and employed as the adsorbents for CO₂ adsorption, demonstrating the decisive effect of ultramicropore and heteroatom doping on CO₂ adsorption capacity. Corn silk, as a cheap and readily available biomass raw material, containing abundant N and O elements [39], is a potential candidate for preparing porous adsorbents toward CO₂ capture, and the adsorption performance of carbon materials based on corn silk has not yet been investigated. Herein, N/O codoped porous carbons were synthesized from corn silk, while pore-structure and surface chemical features were adjusted through Na₂CO₃ activation at high temperatures. The optimized sample, with abundant ultramicropores and pyrrolic N, displays an enhanced CO₂ adsorption capacity, in comparison to its counterparts. This work is expected to pave an accessible pathway for synthesizing a cost-effective alternative that enhances CO₂ capture.

2. Materials and Methods

2.1. Materials

The original corn silk was obtained from a corn field in Daixian, Shanxi province, China. The chemical reagents, such as sulfuric acid (H_2SO_4), hydrochloric acid (HCl), and sodium carbonate (Na_2CO_3) were purchased from Sinopharm Chemical Reagent Co., Ltd., Shanghai, China and used without further purification.

2.2. Fabrication of N/O Codoped Porous Carbons (NOPCs)

The synthesizing process of NOPCs is shown in Figure 1. Typically, corn silks were dispersed in 0.5 M H_2SO_4 solution and maintained at 80 °C for 5 h. The products were treated with 1 M HCl, and subsequently washed with deionized H_2O until neutral. Finally, the silks were dried at 100 °C for 12 h to obtain acid-activated corn silks (a-CS). Next, the a-CS was thoroughly blended with a Na_2CO_3 solution (the weight ratio value of Na_2CO_3 to a-CS is 0:1/1:1/3:1/9:1) and the obtained mixture was impregnated and stirred for 12 h, followed by separation and airing at 100 °C for 24 h. Afterwards, 1 g of the mixture powder was placed in a tube furnace under an N_2 atmosphere and activated at 800 °C for 3 h. Subsequently, the products were soaked in 1 M HCl for 24 h and washed with deionized water until a pH value of seven was reached. Finally, a N/O codoped porous carbon was obtained after drying overnight at 100 °C, which was named NOPCx, where x represented the Na_2CO_3 /a-CS mass ratio.

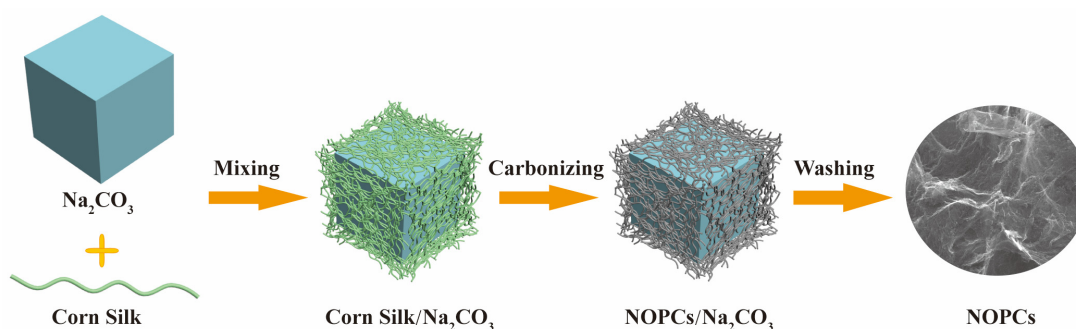


Figure 1. Schematic illustration of fabrication of NOPCs.

2.3. Characterization

The surface morphology and microstructure of NOPCs were observed via scanning electron microscopy (SEM, Thermo Fisher Quattro S, Thermo Fisher Scientific, Waltham, MA, USA) and transmission electron microscopy (TEM, Thermo Scientific Talos F200S, Thermo Fisher Scientific, USA). The crystallinity of samples was characterized via X-ray diffractometer (XRD, Bruker D8 Advance, Bruker, Germany) with Cu-K α radiation ($\lambda = 1.5418 \text{ \AA}$). The graphitization degree of NOPC samples was investigated using a Raman spectrometer (Raman, Thermofisher Dxr2xi, Thermo Fisher Scientific, USA) with an excitation wavelength of 514 nm. The elemental composition of samples was analyzed using an elemental analyzer (EA, Elementar Vario EL cube, Elementar, Germany). The surface functional groups and elemental contents of NOPCs were determined using a Fourier transformed infrared spectrometer (FTIR, Thermo Scientific Nicolet iS50, Thermo Fisher Scientific, USA) and X-ray photoelectron spectroscopy (XPS, Thermo Fisher Scientific K-alpha, Thermo Fisher Scientific, USA) with a monochromatic Al K α X-ray source (1486.6 eV photons). Shirley background subtraction was used for the deconvolution of XPS spectra. The textural properties of NOPCs were measured at 77 K using a gas sorption analyzer (Micromeritics ASAP 2460, Micromeritics, Norcross, GA, USA). The specific surface area and pore size distribution were determined using the BET method and non-local density functional theory (NLDFT).

2.4. CO₂ Adsorption Experiment

The CO₂ and N₂ adsorption isotherms were measured on a Belsorp Max II instrument under pressures of 0–100 kPa. Prior to the adsorption measurement, the samples were degassed at 120 °C for 12 h to remove impurities from the pores.

3. Results

3.1. Physico-Chemical Properties of NOPCs

The morphological features of the NOPCs are shown in Figure 2. The NOPC0 sample directly carbonized from a-CS shows a relatively dense block structure and smooth surface without apparent pores (Figure 2a,b). Compared to NOPC0, the NOPC1 displays a wrinkled flake surface (Figure 2c,d), implying that the new surface with pore structures in the sample can be produced through Na₂CO₃ activation. With the increase of Na₂CO₃ dosage, a large number of pores, even macropores, are observed on the surface (Figure 2e,f). It is worth noting that, NOPC9 exhibits a sponge-like overall structure with multiscale pore holes present (Figure 2g,h), indicating that micropores can be transformed into mesopores and macropores in the cases of higher dosage of Na₂CO₃, which is mainly caused by the escape of a large amount of gas molecules, such as CO or CO₂, during the activation process. In addition, there are no obvious macropores on the flake surface in NOPC1 (Figure 2i), suggesting micropores and mesopores dominated carbon materials. The corresponding HR-TEM image (Figure 2i inset image) shows a heterogeneous worm-like structure with irregular lattice fringes, manifesting the characteristics of amorphous carbon.

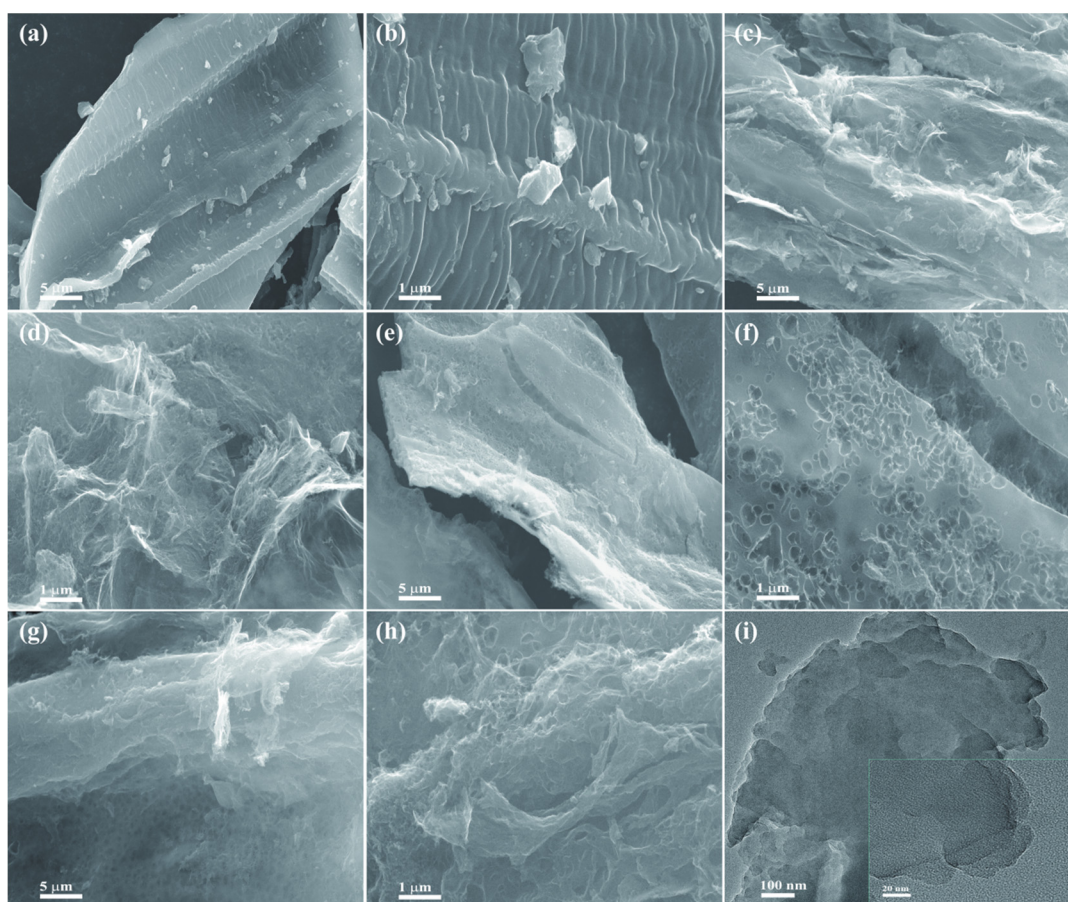


Figure 2. SEM images of (a,b) NOPC0, (c,d) NOPC1, (e,f) NOPC3, (g,h) NOPC9. TEM image of (i) NOPC1 and HR-TEM image of NOPC1 in inset.

The XRD spectra of all samples (Figure 3a) displays two broad peaks at around 24° and 43°, which belong to (002) and (100) plane reflections of carbon, respectively [15,27].

Notably, compared to the unactivated NOPC0, the diffraction peaks of other samples become wider, signifying more defects and disorderly structures. The graphitization degree of all samples was further analyzed via Raman spectra as shown in Figure 3b. Two prominent broad peaks located at approximately 1344 cm^{-1} (D band) and 1575 cm^{-1} (G band) are clearly observed, which is ascribed to amorphous/defective carbon and graphitic carbon, respectively [27,40]. The ratios of D band to G band (I_D/I_G) for NOPC1, NOPC3 and NOPC9 are higher than NOPC0, indicating that more defects were introduced into carbon network by the activation treatment of Na_2CO_3 at high temperatures. In fact, this enhanced degree of disorder can offer more active sites for improving CO_2 adsorption capacity [28,40].

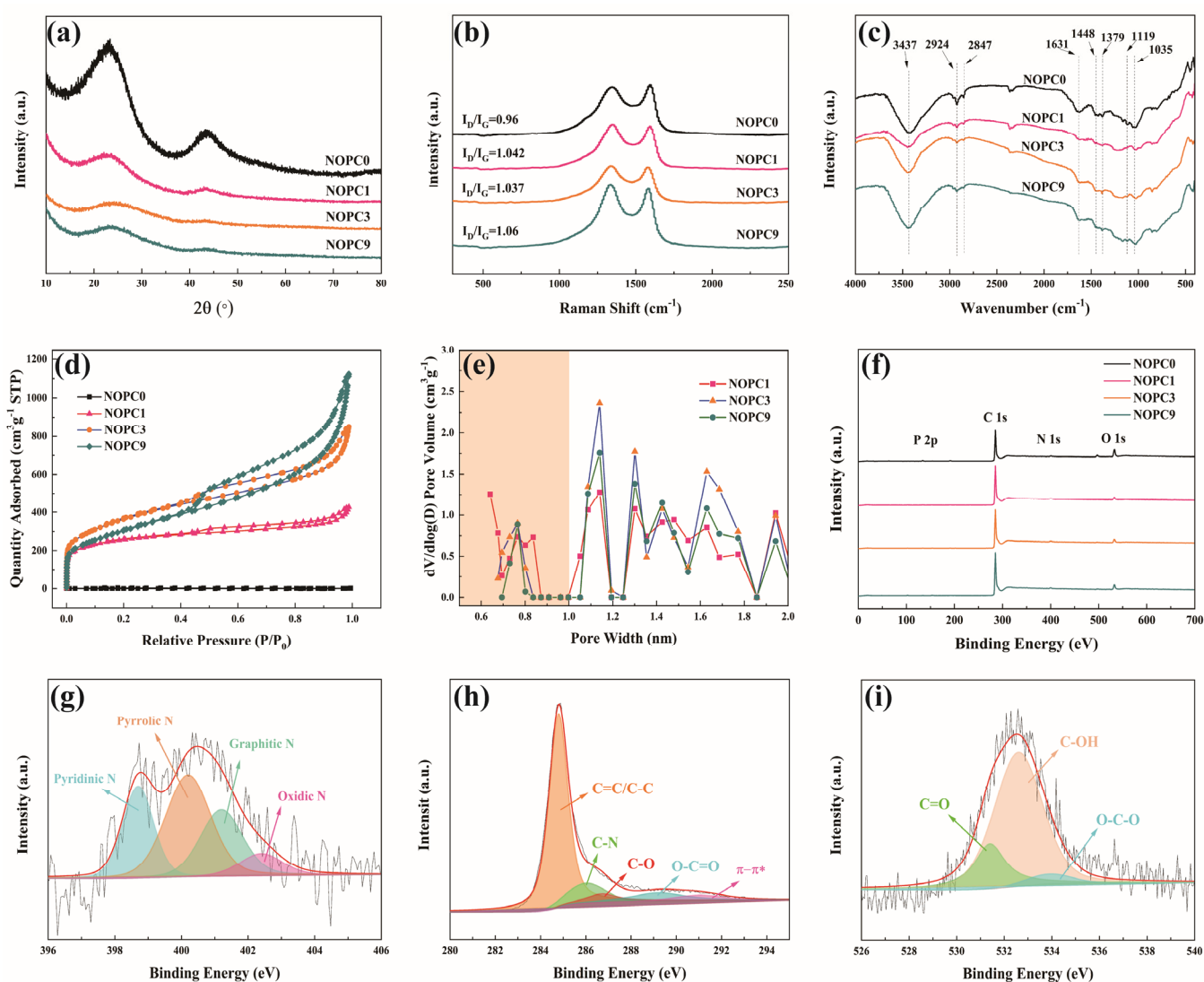


Figure 3. (a) XRD patterns, (b) Raman spectra, (c) FT–IR spectra and (d) N_2 adsorption-desorption isotherms of NOPCs. (e) Pore size distributions of NOPC1, NOPC3 and NOPC9. (f) XPS survey scan for all samples. (g) N 1s spectrum, (h) C 1s and (i) O 1s spectrum of NOPC1.

The surface features of all samples were further analyzed by FT–IR, as illustrated in Figure 3c. The broad band at 3437 cm^{-1} is assigned to O–H and/or N–H stretching vibrations [15,41,42], while two weak peaks at 2924 cm^{-1} and 2847 cm^{-1} are ascribed to the C–H stretching vibrations [40,43]. The moderately intense peak centered at 1631 cm^{-1} belongs to C=C/C–N/C–O [11,15]. Two weak peaks at 1448 and 1119 cm^{-1} are attributed to pyridine-like groups and C–N, respectively [15,41,43]. In addition, the peaks located at 1379 and 1035 cm^{-1} are related to O–H [11,43] and C–O bonds [42], respectively.

The results of the FT–IR analysis clearly confirm that N and O elements are successfully introduced into the carbon skeleton structure through the activation of Na_2CO_3 .

The textural properties of NOPCs are measured via N_2 adsorption-desorption at 77 K, as shown in Figure 3d. The NOPC0 with a non-porous structure exhibits a low BET surface area ($0.47 \text{ m}^2 \text{ g}^{-1}$) and a negligible adsorption capacity. Different from NOPC0, other samples prominently increase in their N_2 adsorption capacity at $P/P_0 < 0.05$ and show an obvious hysteresis loop at $P/P_0 > 0.4$, implying the characteristics of microporous and mesoporous structures [22,28]. In addition, a sharp increase of N_2 uptakes in the high pressures ($0.9 < P/P_0 < 1.0$), suggesting the existence of a small number of macropores [15], testified in Figures 2 and S1. For further analysis, the textural properties of all samples are listed in Table 1. After chemical activation, the specific areas of NOPC1, NOPC3 and NOPC9 are significantly higher than that of NOPC0, verifying the indispensable role of Na_2CO_3 in forming porous structures in carbon materials. Notably, the NOPC9 has lower surface area and pore volumes than NOPC3, which is most likely due to the pore collapse phenomenon caused by higher etching with more dosages of Na_2CO_3 at high temperatures. As summarized in Table 1, the pore size distributions obtained via the NLDFT method show that the cumulative micropore volume of NOPC1 is $0.3668 \text{ cm}^3 \text{ g}^{-1}$, higher than NOPC3 ($0.3618 \text{ cm}^3 \text{ g}^{-1}$) and NOPC9 ($0.2899 \text{ cm}^3 \text{ g}^{-1}$). In addition, the micropore diameters ($< 1 \text{ nm}$) of NOPC1, NOPC3 and NOPC9 are mainly concentrated at 0.8 nm , and the NOPC1 possesses the highest cumulative ultramicropore volume. More impressively, as reflected in Figure 3e and Table 1, the cumulative ultramicropore volume ($< 0.7 \text{ nm}$) for NOPC1 is much larger than that of other samples, which is beneficial for enhancing CO_2 adsorption due to the overlapping interaction of the van der Waals' force [20,27,29,32].

Table 1. Textural properties of all samples.

| Sample | S_{BET} ($\text{m}^2 \text{ g}^{-1}$) | V_t ^a ($\text{cm}^3 \text{ g}^{-1}$) | V_m ^b ($\text{cm}^3 \text{ g}^{-1}$) | V_1 ^c ($\text{cm}^3 \text{ g}^{-1}$) | $V_{0.7}$ ^d ($\text{cm}^3 \text{ g}^{-1}$) |
|--------|--|---|---|---|---|
| NOPC0 | 0.47 | 8.9×10^{-4} | - | - | - |
| NOPC1 | 850.16 | 0.82 | 0.3668 | 0.1795 | 0.1194 |
| NOPC3 | 1269.79 | 1.63 | 0.3618 | 0.1169 | 0.0762 |
| NOPC9 | 1096.95 | 1.42 | 0.2899 | 0.0885 | 0.0604 |

^a: Total pore volume (V_t) obtained at P/P_0 of 0.99. ^{b,c,d}: Cumulative micropore volume of V_m , ($d < 2 \text{ nm}$), V_1 , ($d < 1 \text{ nm}$) and $V_{0.7}$ ($d < 0.7 \text{ nm}$) determined by NLDFT model.

The elemental contents of NOPCs samples were analyzed via EA as listed in Table S1. With the increase of the mass ratio of Na_2CO_3 , the oxygen contents of activated samples display a continuously increasing tendency, while nitrogen contents increase at first, and then decrease. Interestingly, the nitrogen content of NOPC9 is lower than NOPC3, which may be due to the release of nitrogen species by reacting with excessive Na_2CO_3 . In addition, all samples have higher levels of oxygen than nitrogen, revealing that oxygen-containing functional groups are more stable at high temperatures. Considering that all samples retain a considerable amount of N and O, it can be speculated that N and O elements are successfully induced into the carbon backbone. The surface elemental compositions of NOPCs were further determined via XPS. The C, O, N and trace P elements were detected on the surface of all samples, as shown in Figure 3f and Table S2, and the elemental contents of nitrogen and oxygen calculated by XPS results exhibit the same variation pattern as the EA analysis. The deconvolution of N 1s spectra (Figure 3g) for all samples yielded four peaks at binding energies of 398.7, 400.2, 401.2 and 402.4 eV, which are attributed to the pyridinic N, pyrrolic N, graphitic N and oxidized N, respectively [44,45]. The relative contents of different N species and O species for all samples are summarized in Table 2. With the increase in the mass ratio of Na_2CO_3 , the contents of pyridinic N and oxidized N increase significantly, while that of pyrrolic N and graphitic N decrease. In fact, pyrrolic N and pyridinic N play a dominant role in enhancing the CO_2 adsorption performance via Lewis acid-base interactions and hydrogen bonding between surface functional groups and CO_2 molecules [15,19,22,27,41,42]. Therefore, the NOPC1 sample with the highest relative contents of pyrrolic N can be employed as a potential adsorbent

for CO₂ adsorption. In addition, a certain number of oxygen groups in porous carbons can also boost CO₂ adsorption capacity [34,35]. Therefore, the characteristics of oxygen-containing groups are assessed by the high-resolution C 1s and O 1s spectra, as described in Figure 3h,i. The high-resolution C 1s spectroscopy shows five major peaks, corresponding to C=C/C–C (284.8 eV), C–N (286.0 eV), C–O (286.7 eV), O–C=O (289.2 eV) and π – π^* bonds (291.0 eV), respectively [46,47]. Likewise, the O 1s spectra can be fitted into three peaks located at 531.4 eV, 532.6 eV and 533.9 eV, corresponding to C=O, C–OH and C–O–C, respectively [44,48]. These XPS results confirm the existence of abundant oxygen-containing functional groups on the surface of NOPC samples, which is beneficial for further promoting CO₂ adsorption [16,29,43]. More significantly, the NOPC1 sample has the highest content of C–OH among NOPCs, as listed in Table 2, suggesting a stronger affinity for CO₂ through the hydrogen bonding interactions [21].

Table 2. The contents of different N species and O species for NOPCs samples.

| Sample | N Species (%) | | | | O Species (%) | | |
|--------|-----------------|----------------|-----------------|----------------|---------------|----------|-----------|
| | Pyridinic N (%) | Pyrrolic N (%) | Graphitic N (%) | Oxidized N (%) | C=O (%) | C–OH (%) | C–O–C (%) |
| NOPC0 | 27.26 | 41.34 | 22.07 | 9.34 | 14.97 | 64.77 | 20.26 |
| NOPC1 | 25.55 | 41.21 | 24.98 | 8.27 | 15.24 | 79.53 | 5.23 |
| NOPC3 | 29.37 | 38.01 | 19.54 | 13.08 | 20.3 | 75.38 | 4.32 |
| NOPC9 | 32.21 | 34.31 | 18.49 | 15 | 16.18 | 75.92 | 7.89 |

3.2. CO₂ Adsorption Performance of NOPCs

The CO₂ adsorption capacity of NOPC1, NOPC3 and NOPC9 were measured at 273 K and 298 K under 1 bar, respectively. As displayed in Figure 4a,b, the CO₂ adsorption uptakes of all samples significantly decrease as the temperature is increased from 273 K to 298 K, verifying the exothermic adsorption characteristic in thermodynamics. It is noteworthy that NOPC1, with the lowest specific surface area, exhibits the highest CO₂ uptakes (3.15 and 1.95 mmol g^{−1} at 273 K and 298 K, respectively, Table 3). To demonstrate these results, the relationships between CO₂ uptake and the physicochemical characteristics are investigated and shown in Figure 4c and Figure S2. It can be seen that the CO₂ uptake is positively correlated with the V₁ (d < 1 nm), V_{0.7} (d < 0.7 nm) and content of pyrrolic N, however, it is rarely related to BET surface area, nitrogen content and micropore volume. In fact, when the slit pore (below 0.7 nm) is smaller than twice the kinetic diameter of CO₂ molecules (0.33 nm), the interaction between CO₂ and adsorbent surfaces can be enhanced through the van der Waals force [20]. Additionally,, as listed in Table 2, the higher contents of pyrrolic N and C–OH in NOPC1 can strengthen the affinity for CO₂ molecules, thereby effectively improving its CO₂ adsorption capacity. Numerous studies have claimed that ultramicropores (d < 0.7 nm) play the decisive role in enhancing CO₂ adsorption compared to other factors [32,35,36,49]. More comparisons of the CO₂ adsorption capacity of NOPC1 and other activated carbon materials are listed in Table 4. The NOPC1 sample in our work exhibits competitive CO₂ adsorption performance compared to other adsorbents in previous studies.

Table 3. CO₂ and N₂ uptakes, and CO₂/N₂ selectivity of NOPC1, NOPC3 and NOPC9.

| Sample | CO ₂ Uptake (mmol g ^{−1}) | | N ₂ Uptake (mmol g ^{−1}) | CO ₂ /N ₂ Selectivity (298 K) | |
|--------|--|-------|---|---|-------------|
| | 273 K | 298 K | 298 K | IAST (1 bar) | Henry's Law |
| NOPC1 | 3.15 | 1.95 | 0.196 | 16.9 | 15.6 |
| NOPC3 | 2.63 | 1.55 | 0.223 | 8.8 | 10.2 |
| NOPC9 | 2.17 | 1.27 | 0.145 | 12.2 | 16.0 |

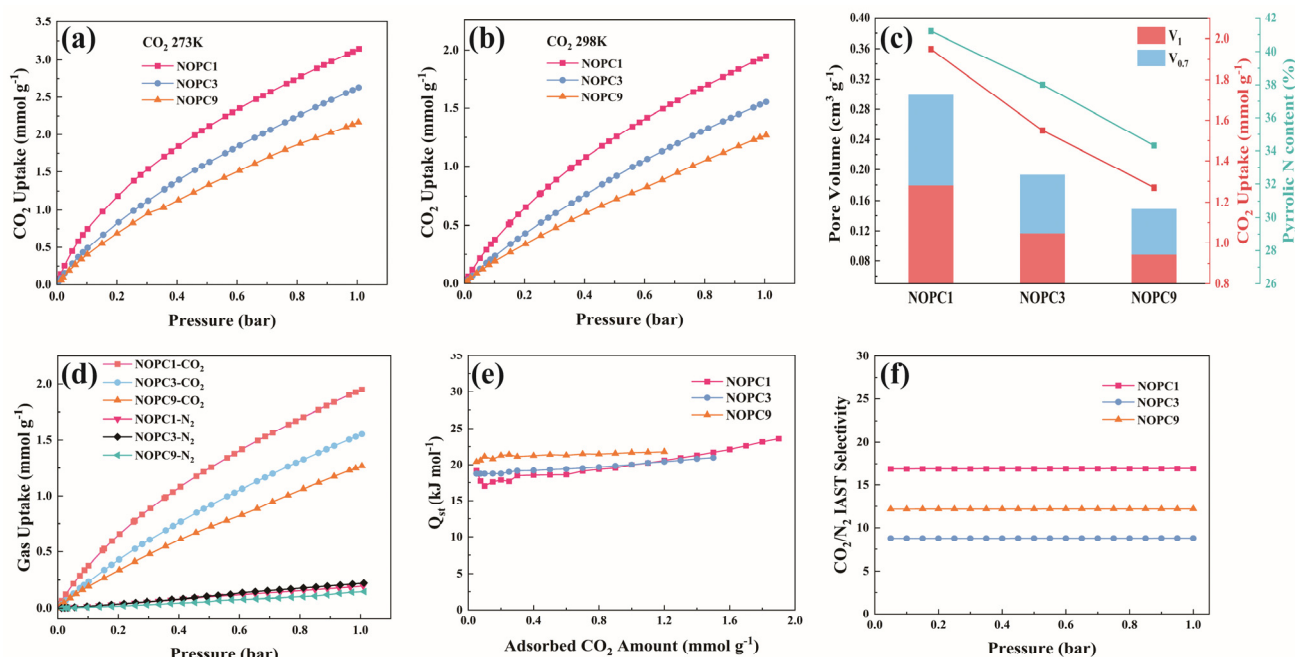


Figure 4. CO₂ adsorption isotherms of NOPC1, NOPC3 and NOPC9 at (a) 273 K and (b) 298 K. (c) The relationship of CO₂ uptake with ultramicropore volume and pyrrolic N content. (d) Isothermic heat of CO₂ adsorption for NOPC1, NOPC3 and NOPC9. (e) Isotherms of CO₂ and N₂ of NOPC1, NOPC3 and NOPC9 at 298 K. (f) CO₂/N₂ IAST selectivity of NOPC1, NOPC3 and NOPC9 at 298 K.

Table 4. CO₂ adsorption performance of NOPC1 compared with other works.

| Sample | Activation | S _{BET} (m ² g ⁻¹) | CO ₂ Uptake (mmol g ⁻¹) (298 K, 1 Bar) | IAST Selectivity | Ref. |
|--------------|---|---|---|---------------------|-----------|
| A-TDP-12 | KOH, 700 °C | 1332 | 1.52 | 6 | [28] |
| C0800 | 800 °C | 431 | 2.4 | 33.7 | [31] |
| C2800 | hydroquinonesulfonic acid potassium salt, 800 °C | - | 1.9 | 12.5 | [31] |
| AC-TBG | KOH, 800 °C | 971 | 3.2 | - | [33] |
| AC-UK | KOH, 650 °C | 532 | 2.63 | - | [34] |
| SRC-3K-500 | KOH, 500 °C | 743 | 2.78 | 6.7 | [50] |
| Z0800 | Zn(NO ₃) ₂ , 800 °C | 569 | 2.5 | 25.0 | [51] |
| 1:2/900/2 | H ₃ PO ₄ , 800 °C | 773 | 1.88 | - | [52] |
| A-TCLP-700-1 | KOH, 700 °C | 1353 | 2.39 | 19 | [53] |
| NOPC1 | Na ₂ CO ₃ , 500 °C | 850.16 | 1.95 | 16.9 | This work |

Isosteric heat adsorption (Q_{st}) is a significant thermodynamic parameter to evaluate the affinity of adsorbents for CO₂. To determine the value of Q_{st} , the pure adsorption isotherms of CO₂ on NOPCs are first fitted using the single-site Langmuir model [54,55]:

$$q = \frac{q_{sat}bp}{1 + bp} \quad (1)$$

where q is the adsorption capacity (mmol g⁻¹), q_{sat} presents saturation adsorption capacity (mmol g⁻¹), b is Langmuir constant (kPa⁻¹), and p is the pressure (kPa). Next, Q_{st} can be calculated based on the fitted CO₂ adsorption data at 273 and 298 K via the Clausius-Clapeyron equation [27]:

$$Q_{st} = -RT^2 \left(\frac{\partial \ln P}{\partial T} \right) \quad (2)$$

where R , P and T represent the gas constant (8.314 J mol⁻¹ K⁻¹), pressure (kPa) and temperature (K), respectively. From Figure 4d, it is calculated that the Q_{st} values of all samples are in the range of 18.7–23.6 kJ mol⁻¹, implying the physisorption mechanism of the adsorption process [15]. Notably, the Q_{st} values of all adsorbents exhibit a slight increase with

the improved adsorption capacity, which may be attributed to the enhanced adsorbate-adsorbate interactions between CO₂ molecules in the ultramicropore [22,27]. In substance, CO₂ molecules preferentially occupy the active sites during the adsorption process, and as the amount of CO₂ increased, the ultramicropore ($d < 0.7$ nm) played the dominant role [27,56]. The higher Q_{st} for NOPC9 at low CO₂ loading is most likely due to its higher content of oxygen-containing functional groups (Tables S1 and S2), which provide more active adsorption sites. Furthermore, at high surface coverage, the value of Q_{st} for NOPC1 is higher than those for NOPC3 and NOPC9, verifying the decisive effect of ultramicropores ($d < 0.7$ nm) enhancing the affinity of adsorbents for CO₂.

Moreover, the CO₂/N₂ selectivity is a significant parameter to determine the practical applications of adsorbents. Figure 4e shows the CO₂ and N₂ adsorption uptakes of NOPC1, NOPC3 and NOPC9 at 298 K. The CO₂ adsorption uptakes are significantly higher than the N₂ adsorption uptakes over the entire pressure range at 298 K, demonstrating the higher adsorption selectivity of as-prepared samples for CO₂, which is in favor of separating CO₂ from combustion flue gas. To further evaluate the performance of adsorbents, the CO₂/N₂ adsorption selectivity can be calculated by the ideal adsorption solution theory (IAST) using CO₂ and N₂ adsorption data fitted with a single-site Langmuir model (Equation (1)). The main components of flue gas are assumed to be N₂ (85%) and CO₂ (15%). The IAST selectivity (S) can be defined as [55,57]:

$$S = \frac{x_1/y_1}{x_2/y_2} \quad (3)$$

where x and y represent the mole fraction of different components in the adsorbed phase mixture and the gas phase mixture, respectively. Next, the IAST selectivity of CO₂/N₂ for NOPC1, NOPC3 and NOPC9 at 298 K was calculated according to the IAST method and presented in Figure 4f and Table 3. It is found that the IAST selectivity of NOPC1 is much higher than those of NOPC3 and NOPC9. In addition, the CO₂/N₂ selectivity is also estimated using Henry's law (Supporting information) and the corresponding results are summarized in Table 3. The CO₂/N₂ selectivity determined by two theoretical models turn in a consistent performance. Significantly, the NOPC1 sample with the highest selectivity may benefit from its higher ratio of ultramicropores (Figure 3e and Table 1), since the deep well potential in the ultramicropore wall can thoroughly soak CO₂ molecules and increase the adsorption potential energy, thereby boosting the CO₂ adsorption selectivity [27,49]. On the other hand, the CO₂/N₂ selectivity of NOPC9 is significantly higher than that of NOPC3, which is most likely due to the fact that abundant oxygen-contained functional groups on the surface of NOPC9 enhance interactions with CO₂ molecules.

4. Conclusions

In summary, NOPCs were fabricated via direct carbonization of corn silk involving Na₂CO₃ activators. The obtained NOPC1 sample has a large specific surface, high ultramicropore volume ($d < 0.7$ nm and $d < 1$ nm) and high content of pyrrolic N. Therefore, NOPC1 provides 3.15 and 1.95 mmol g⁻¹ of the CO₂ uptake at 273 K and 298 K under 1 bar, respectively. Additionally, the CO₂/N₂ selectivity determined by the IAST model and Henry's law is 16.9 and 15.6 at 298 K, respectively. It has been demonstrated that ultramicropore and pyrrolic N exert greater influence on the CO₂ adsorption capacity and CO₂/N₂ selectivity. Notably, the CO₂ adsorption capacity of NOPCs needs to be further improved and the essential factor (ultramicropore and pyrrolic N) for enhancing the CO₂ adsorption performance cannot be independently studied in this work. However, the current research provides valuable information on synthesis of N/O codoped carbon adsorbents derived from biomass for selective CO₂ adsorption.

Supplementary Materials: The following supporting information can be downloaded at: <https://www.mdpi.com/article/10.3390/en16135222/s1>, Figure S1: Pore size distribution curves of NOPC1, NOPC3 and NOPC9. Figure S2: The linear fitting of CO₂ uptake (298 K, 1 bar) against (a) BET surface area, (b) Nitrogen content, (c) Pyrrolic N content, (d) V_m, (e) V₁ and (f) V_{0.7}. Figure S3: The CO₂/N₂ selectivity by Henry's law on NOPC1 (a), NOPC3 (b) and NOPC9 (c) at 298 K. Table S1: The elemental composition of NOPCs analyzed by EA. Table S2: The surface elemental composition of NOPCs calculated by XPS results.

Author Contributions: C.G.: conceptualization, methodology, resources, data analysis, formal analysis, funding acquisition, writing—original draft. Y.S.: data analysis. H.R.: resources, supervision. B.W.: formal analysis, funding acquisition, supervision. X.T.: formal analysis, supervision. X.W.: funding acquisition, supervision. Y.N.: funding acquisition, supervision. J.W.: formal analysis, supervision. All authors have read and agreed to the published version of the manuscript.

Funding: This work was funded by Science and Technology Innovation Project of Shanxi Colleges and Universities, China (2021L014 and 2021L006) and the Applied Basic Research Project of Shanxi province, China (20210302124126 and 202103021223031).

Data Availability Statement: Not applicable.

Conflicts of Interest: The authors declare no conflict of interest.

References

1. Jahromi, F.B.; Elhambakhsh, A.; Keshavarz, P.; Panahi, F. Insight into the application of amino acid-functionalized MIL-101 (Cr) micro fluids for high-efficiency CO₂ absorption: Effect of amine number and surface area. *Fuel* **2023**, *334*, 126603. [CrossRef]
2. Xin, K.; Annaland, M.V.S. Diffusivities and solubilities of carbon dioxide in deep eutectic solvents. *Sep. Purif. Technol.* **2023**, *307*, 122779. [CrossRef]
3. Pazani, F.; Shariatifar, M.; Maleh, M.S.; Alebrahim, T.; Lin, H.Q. Challenge and promise of mixed matrix hollow fiber composite membranes for CO₂ separations. *Sep. Purif. Technol.* **2023**, *308*, 122876. [CrossRef]
4. Park, K.H.; Lee, J.W.; Lim, Y.; Seo, Y. Life cycle cost analysis of CO₂ compression processes coupled with a cryogenic distillation unit for purifying high-CO₂ natural gas. *J. CO₂ Util.* **2022**, *60*, 102002. [CrossRef]
5. Wang, L.; Yao, Y.; Tran, T.; Lira, P.; Sternberg, S.P.E.; Davis, R.; Sun, Z.; Lai, Q.H.; Toan, S.; Luo, J.M.; et al. Mesoporous MgO enriched in Lewis base sites as effective catalysts for efficient CO₂ capture. *J. Environ. Manag.* **2023**, *332*, 117398. [CrossRef]
6. Cui, H.M.; Xu, J.G.; Shi, J.S.; Yan, N.F.; Zhang, C.; You, S.Y. Oxamic acid potassium salt as a novel and bifunctional activator for the preparation of N-doped carbonaceous CO₂ adsorbents. *J. CO₂ Util.* **2022**, *64*, 102198. [CrossRef]
7. Ma, C.D.; Bai, J.L.; Demir, M.; Yu, Q.Y.; Hu, X.; Jiang, W.H.; Wang, L.L. Polyacrylonitrile-derived nitrogen enriched porous carbon fiber with high CO₂ capture performance. *Sep. Purif. Technol.* **2022**, *303*, 122299. [CrossRef]
8. Cavallo, M.; Dosa, M.; Porcaro, N.G.; Bonino, F.; Piumetti, M.; Crocella, V. Shaped natural and synthetic zeolites for CO₂ capture in a wide temperature range. *J. CO₂ Util.* **2023**, *67*, 102335. [CrossRef]
9. Song, K.S.; Fritz, P.W.; Coskun, A. Porous organic polymers for CO₂ capture, separation and conversion. *Chem. Soc. Rev.* **2022**, *51*, 9831. [CrossRef]
10. Al-Absi, A.A.; Mohamedali, M.; Domin, A.; Benneker, A.M.; Mahinpey, N. Development of in situ polymerized amines into mesoporous silica for direct air CO₂ capture. *Chem. Eng. J.* **2022**, *447*, 137465. [CrossRef]
11. Sun, H.F.; Zhang, Q.G.; Hagio, T.; Ryoichi, I.; Kong, L.; Li, L. Facile synthesis of amine-functionalized three-dimensional graphene composites for CO₂ capture. *Surf. Interfaces* **2022**, *33*, 102256. [CrossRef]
12. Zhu, W.F.; Wang, L.Z.; Cao, H.H.; Guo, R.L.; Wang, C.F. Introducing defect-engineering 2D layered MOF nanosheets into Pebax matrix for CO₂/CH₄ separation. *J. Membr. Sci.* **2023**, *669*, 121305. [CrossRef]
13. Ding, M.L.; Robinson, W.F.; Jiang, H.L.; Yaghi, O.M. Carbon capture and conversion using metal-organic frameworks and MOF-based materials. *Chem. Soc. Rev.* **2019**, *48*, 2783–2828. [CrossRef]
14. Yang, L.X.; Yang, H.; Wu, H.; Zhang, L.L.; Ma, H.Z.; Liu, Y.T.; Wu, Y.Z.; Ren, Y.X.; Wu, X.Y.; Jiang, Z.Y. COF membranes with uniform and exchangeable facilitated transport carriers for efficient carbon capture. *J. Mater. Chem. A* **2021**, *9*, 12636. [CrossRef]
15. Yuan, X.F.; Xiao, J.F.; Yilmaz, M.; Zhang, T.C.; Yuan, S.J. N, P Co-doped porous biochar derived from cornstalk for high performance CO₂ adsorption and electrochemical energy storage. *Sep. Purif. Technol.* **2022**, *299*, 121719. [CrossRef]
16. Lu, T.Y.; Ma, C.D.; Demir, M.; Yu, Q.Y.; Aghamohammadi, P.; Wang, L.L.; Hu, X. One-pot synthesis of potassium benzoate-derived porous carbon for CO₂ capture and supercapacitor application. *Sep. Purif. Technol.* **2022**, *301*, 122053. [CrossRef]
17. Petrovic, B.; Gorbounov, M.; Soltani, S.M. Influence of surface modification on selective CO₂ adsorption: A technical review on mechanisms and methods. *Microporous Mesoporous Mater.* **2021**, *312*, 110751. [CrossRef]
18. Hakami, O. Urea-doped hierarchical porous carbons derived from sucrose precursor for highly efficient CO₂ adsorption and separation. *Surf. Interfaces* **2023**, *37*, 102668. [CrossRef]
19. Shen, Y.F. Preparation of renewable porous carbons for CO₂ capture—A review. *Fuel Process. Technol.* **2022**, *236*, 107437. [CrossRef]

20. Liu, B.G.; Shi, R.; Ma, X.C.; Chen, R.F.; Zhou, K.; Xu, X.; Sheng, P.; Zeng, Z.; Li, L.Q. High yield nitrogen-doped carbon monolith with rich ultramicropores prepared by in-situ activation for high performance of selective CO₂ capture. *Carbon* **2021**, *181*, 270–279. [[CrossRef](#)]
21. Guo, Z.; Lu, X.; Xin, Z. N, S, O co-doped porous carbons derived from bio-based polybenzoxazine for efficient CO₂ capture. *Colloid Surf. A* **2022**, *646*, 128845. [[CrossRef](#)]
22. Zhou, Y.B.; Tan, P.; He, Z.Q.; Zhang, C.; Fang, Q.Y.; Chen, G. CO₂ adsorption performance of nitrogen-doped porous carbon derived from licorice residue by hydrothermal treatment. *Fuel* **2022**, *311*, 122507. [[CrossRef](#)]
23. Cui, H.J.; Jiao, M.G.; Chen, Y.N.; Guo, Y.B.; Yang, L.P.; Xie, Z.J.; Zhou, Z.; Guo, S.J. Molten-salt-assisted synthesis of 3D holey N-doped graphene as bifunctional electrocatalysts for rechargeable Zn-Air batteries. *Small Methods* **2018**, *2*, 1800144. [[CrossRef](#)]
24. Caglayan, B.S.; Aksoylu, A.E. CO₂ adsorption on chemically modified activated carbon. *J. Hazard. Mater.* **2013**, *252–253*, 19–28. [[CrossRef](#)]
25. Li, C.F.; Zhao, J.W.; Xie, L.J.; Wang, Y.; Tang, H.B.; Zheng, L.R.; Li, G.R. N coupling with S-coordinated Ru nanoclusters for highly efficient hydrogen evolution in alkaline media. *J. Mater. Chem. A* **2021**, *9*, 12659–12669. [[CrossRef](#)]
26. Wang, Y.C.; Shao, Y.; Wang, H.; Yuan, J.Y. Advanced heteroatom-doped porous carbon membranes assisted by poly(ionic liquid) design and engineering. *Acc. Mater. Res.* **2020**, *1*, 16–29. [[CrossRef](#)]
27. Chen, C.; Zhang, Y.K.; Li, Q.H.; Wang, Y.L.; Ma, J. Guanidine-embedded poly (ionic liquid) as a versatile precursor for self-templated synthesis of nitrogen-doped carbons: Tailoring the microstructure for enhanced CO₂ capture. *Fuel* **2022**, *329*, 125357. [[CrossRef](#)]
28. Wang, Y.; Xiao, J.F.; Wang, H.Z.; Zhang, T.C.; Yuan, S.J. Binary doping of nitrogen and phosphorus into porous carbon: A novel di-functional material for enhancing CO₂ capture and super-capacitance. *J. Mater. Sci. Technol.* **2022**, *99*, 73–81. [[CrossRef](#)]
29. Yuan, J.C.; Wang, Y.; Tang, M.F.; Hao, X.D.; Liu, J.; Zhang, G.J.; Zhang, Y.F. Preparation of N, O co-doped carbon nanotubes and activated carbon composites with hierarchical porous structure for CO₂ adsorption by coal pyrolysis. *Fuel* **2023**, *333*, 126465. [[CrossRef](#)]
30. Rehman, A.; Nazir, G.; Rhee, K.Y.; Park, S.J. A rational design of cellulose-based heteroatom-doped porous carbons: Promising contenders for CO₂ adsorption and separation. *Chem. Eng. J.* **2021**, *420*, 130421. [[CrossRef](#)]
31. Shi, J.S.; Cui, H.M.; Xu, J.G.; Yan, N.F.; Zhang, C.; You, S.Y. Synthesis of nitrogen and sulfur co-doped carbons with chemical blowing method for CO₂ adsorption. *Fuel* **2021**, *305*, 121505. [[CrossRef](#)]
32. Ma, X.C.; Yang, Y.H.; Wu, Q.D.; Liu, B.G.; Li, D.P.; Chen, R.F.; Wang, C.H.; Li, H.L.; Zeng, Z.; Li, L.Q. Underlying mechanism of CO₂ uptake onto biomass-based porous carbons: Do adsorbents capture CO₂ chiefly through narrow micropores? *Fuel* **2020**, *282*, 118727. [[CrossRef](#)]
33. Prasankumar, T.; Salpekar, D.; Bhattacharyya, S.; Manoharan, K.; Yadav, R.M.; Mata, M.A.C.; Miller, K.A.; Vajtai, R.; Jose, S.; Roy, S.; et al. Biomass derived hierarchical porous carbon for supercapacitor application and dilute stream CO₂ capture. *Carbon* **2022**, *199*, 249–257. [[CrossRef](#)]
34. Dilokekunakul, W.; Teerachawanwong, P.; Klomkliang, N.; Supasitmongkol, S.; Chaemchuen, S. Effects of nitrogen and oxygen functional groups and pore width of activated carbon on carbon dioxide capture: Temperature dependence. *Chem. Eng. J.* **2020**, *389*, 124413. [[CrossRef](#)]
35. Ma, X.C.; Su, C.Q.; Liu, B.G.; Wu, Q.D.; Zhou, K.; Zeng, Z.; Li, L.Q. Heteroatom-doped porous carbons exhibit superior CO₂ capture and CO₂/N₂ selectivity: Understanding the contribution of functional groups and pore structure. *Sep. Purif. Technol.* **2021**, *259*, 118065. [[CrossRef](#)]
36. Li, Q.; Lu, T.Y.; Wang, L.L.; Pang, R.X.; Shao, J.W.; Liu, L.L.; Hu, X. Biomass based N-doped porous carbons as efficient CO₂ adsorbents and high-performance supercapacitor electrodes. *Sep. Purif. Technol.* **2021**, *275*, 119204. [[CrossRef](#)]
37. Ma, C.D.; Lu, T.Y.; Shao, J.W.; Huang, J.M.; Hu, X.; Wang, L.L. Biomass derived nitrogen and sulfur co-doped porous carbons for efficient CO₂ adsorption. *Sep. Purif. Technol.* **2022**, *281*, 119899. [[CrossRef](#)]
38. Mallesh, D.; Anbarasan, J.; Kumar, P.M.; Upendar, K.; Chandrashekar, P.; Rao, B.V.S.K.; Lingaiah, N. Synthesis, characterization of carbon adsorbents derived from waste biomass and its application to CO₂ capture. *Appl. Surf. Sci.* **2020**, *530*, 147226. [[CrossRef](#)]
39. Zhang, Y.L.; Zhao, R.; Li, Y.Q.; Zhu, X.X.; Zhang, B.; Lang, X.Y.; Zhao, L.J.; Jin, B.; Zhu, Y.F.; Jiang, Q. Potassium-ion batteries with novel N, O enriched corn silk-derived carbon as anode exhibiting excellent rate performance. *J. Power Sources* **2021**, *481*, 228644. [[CrossRef](#)]
40. Ruan, W.; Wang, Y.; Liu, C.R.; Xu, D.W.; Hu, P.; Ye, Y.Y.; Wang, D.C.; Liu, Y.Q.; Zheng, Z.F.; Wang, D. One-step fabrication of N-doped activated carbon by NH₃ activation coupled with air oxidation for supercapacitor and CO₂ capture applications. *J. Ana. Appl. Pyrol.* **2022**, *168*, 105710. [[CrossRef](#)]
41. Xiao, J.F.; Yuan, X.F.; Zhang, T.C.; Ouyang, L.K.; Yuan, S.J. Nitrogen-doped porous carbon for excellent CO₂ capture: A novel method for preparation and performance evaluation. *Sep. Purif. Technol.* **2022**, *298*, 121602. [[CrossRef](#)]
42. Jin, Z.H.; Jiang, X.; Dai, Z.D.; Xie, L.L.; Wang, W.; Shen, L. Continuous synthesis of nanodroplet-templated, N-doped microporous carbon spheres in microfluidic system for CO₂ capture. *ACS Appl. Mater. Interfaces* **2020**, *12*, 52571–52580. [[CrossRef](#)]
43. Wu, D.W.; Liu, J.; Yang, Y.J.; Zheng, Y. Nitrogen/oxygen co-doped porous carbon derived from biomass for low-pressure CO₂ capture. *Ind. Eng. Chem. Res.* **2020**, *59*, 14055–14063. [[CrossRef](#)]

44. Xin, S.S.; Huo, S.Y.; Zhang, C.L.; Ma, X.M.; Liu, W.J.; Xin, Y.J.; Gao, M.C. Coupling nitrogen/oxygen self-doped biomass porous carbon cathode catalyst with CuFeO₂/biochar particle catalyst for the heterogeneous visible-light driven photo-electro-Fenton degradation of tetracycline. *Appl. Catal. B* **2022**, *305*, 121024. [[CrossRef](#)]
45. Guo, J.R.; Xu, X.T.; Hill, J.P.; Wang, L.P.; Dang, J.J.; Kang, Y.Q.; Li, Y.L.; Guan, W.S.; Yamauchi, Y. Graphene-carbon 2D heterostructures with hierarchically-porous P, N-doped layered architecture for capacitive deionization. *Chem. Sci.* **2021**, *12*, 10334–10340. [[CrossRef](#)] [[PubMed](#)]
46. Khandelwal, M.; Tran, C.V.; In, J.B. Nitrogen and phosphorous co-doped laser-induced graphene: A high-performance electrode material for supercapacitor applications. *Appl. Surf. Sci.* **2022**, *576*, 151714. [[CrossRef](#)]
47. Ren, G.Y.; Li, Y.N.; Chen, Q.S.; Qian, Y.; Zheng, J.G.; Zhu, Y.A.; Teng, C. Sepia-derived N, P co-doped porous carbon spheres as oxygen reduction reaction electrocatalyst and supercapacitor. *ACS Sustain. Chem. Eng.* **2018**, *6*, 16032–16038. [[CrossRef](#)]
48. Zhu, C.W.; Yan, J.J. Fabricating of N/O-codoping porous carbon interpenetrating networks for high energy aqueous supercapacitor. *J. Energy Storage* **2022**, *52*, 105047. [[CrossRef](#)]
49. Wang, Y.H.; Wang, M.H.; Wang, Z.W.; Wang, S.M.; Fu, J.W. Tunable-quaternary (N, S, O, P)-doped porous carbon microspheres with ultramicropores for CO₂ capture. *Appl. Surf. Sci.* **2020**, *507*, 145130. [[CrossRef](#)]
50. Li, D.N.; Yang, J.Z.; Zhao, Y.; Yuan, H.R.; Chen, Y. Ultra-highly porous carbon from wasted soybean residue with tailored porosity and doped structure as renewable multi-purpose absorbent for efficient CO₂, toluene and water vapor capture. *J. Clean. Prod.* **2022**, *337*, 130283. [[CrossRef](#)]
51. Cui, H.M.; Xu, J.G.; Shi, J.S.; Yan, N.F.; Liu, Y.W.; Zhang, S.W. Zinc nitrate as an activation agent for the synthesis of nitrogen-doped porous carbon and its application in CO₂ adsorption. *Energy Fuels* **2020**, *34*, 6069–6076. [[CrossRef](#)]
52. Botomé, M.L.; Poletto, P.; Junges, J.; Perondi, D.; Dettmer, A.; Godinho, M. Preparation and characterization of a metal-rich activated carbon from CCA-treated wood for CO₂ capture. *Chem. Eng. J.* **2017**, *321*, 614–621. [[CrossRef](#)]
53. Wang, Y.; Xiao, J.F.; Wang, H.Z.; Zhang, T.C.; Yuan, S.J. N-doped porous carbon derived from solvent-free synthesis of cross-linked triazine polymers for simultaneously achieving CO₂ capture and supercapacitors. *Chem. Eur. J.* **2021**, *27*, 7908–7914. [[CrossRef](#)] [[PubMed](#)]
54. Fu, Z.Y.; Jia, J.Z.; Li, J.; Liu, C.K. Transforming waste expanded polystyrene foam into hyper-crosslinked polymers for carbon dioxide capture and separation. *Chem. Eng. J.* **2017**, *323*, 557–564. [[CrossRef](#)]
55. Shao, L.S.; Sang, Y.F.; Liu, N.; Liu, J.; Zhan, P.; Huang, J.H.; Chen, J.N. Selectable microporous carbons derived from poplar wood by three preparation routes for CO₂ capture. *ACS Omega* **2020**, *5*, 17450–17462. [[CrossRef](#)]
56. Wang, Z.; Goyal, N.; Liu, L.Y.; Tsang, D.C.W.; Shang, J.; Liu, W.J.; Li, G. N-doped porous carbon derived from polypyrrole for CO₂ capture from humid flue gases. *Chem. Eng. J.* **2020**, *396*, 125376. [[CrossRef](#)]
57. Krishna, R.; Baten, J.M.V. Elucidation of selectivity reversals for binary mixture adsorption in microporous adsorbents. *ACS Omega* **2020**, *5*, 9031–9040. [[CrossRef](#)]

Disclaimer/Publisher's Note: The statements, opinions and data contained in all publications are solely those of the individual author(s) and contributor(s) and not of MDPI and/or the editor(s). MDPI and/or the editor(s) disclaim responsibility for any injury to people or property resulting from any ideas, methods, instructions or products referred to in the content.